Journal of Applied Fluid Mechanics, Vol. 18, No. 9, pp. 2309-2320, 2025.
Available online at www.jafmonline.net, ISSN 1735-3572, EISSN 1735-3645.
https://doi.org/10.47176/jafm.18.9.3322

Effect of Baffle Structure for the Particle Deposition Characteristics of in the Novel Cavity Upstream of the Pre-swirl Nozzles

Y. Wang†, G. C. Li, W. Zhang, and H. B. He

School of Aero-engine, Shenyang Aerospace University, Shenyang, Liaoning, 110136, China

†*Corresponding Author Email: wangyan1@stu.sau.edu.cn*

ABSTRACT

This study investigates the particle deposition characteristics within a novel cavity featuring a transverse baffle oriented perpendicular to the coolant flow, positioned upstream of the pre-swirl nozzles in the turbine disk cavity. The baffle-induced vortex enhances particle deposition, thereby reducing particle ingress into the turbine disk cavity. Against such a background, a comparative analysis was hereby conducted to delve into the deposition characteristics of particles across four baffle structures. The coolant and particle temperature at the cavity inlet was set at 763.5 K, with a total coolant mass flow rate of 0.2475 kg/s through two impingement holes and an outlet pressure of 2 MPa. The results indicate that the quantity-based deposition rate increases from 66.4% prior to the installation of baffle to 77.2% following the implementation of three baffles. Furthermore, the quality-based deposition rate rises from 14.7% in the absence of baffles to 37.2% following the installation of three baffles. The deposition is primarily concentrated in the target surface area directly opposite the impingement hole, between Baffle 1, and in regions located at 0.5 times the diameter of the impingement hole both upstream and downstream of Baffle 3.

Article History

Received December 16, 2024
Revised March 24, 2025
Accepted April 11, 2025
Available online July 5, 2025

Keywords:

Baffle structure
Novel cavity
Pre-swirl nozzles
Particle deposition
Turbine disk

1. INTRODUCTION

Since the 21st century, the phenomenon of particle accumulation in aerospace engines has garnered substantial attention from the academic community. Studies have indicated that, under normal flight conditions, the concentration of particles entering the engine typically falls within the range of 0.1% to 2%. This proportion may increase significantly during extreme weather events or when operating in areas affected by sandstorms. Particles ingress into the engine induces compressor wear and deteriorates aerodynamic performance (Felix et al., 2017). Furthermore, these particles pose risks to other engine components, with the most pronounced effects observed on turbine blades. On the one hand, particle deposition may modify blade surface smoothness, disrupt airflow, increase aerodynamic resistance, and consequently diminish turbine efficiency. On the other, particles tend to accumulate within the cooling passages of the turbine blades, thereby adversely impacting internal cooling performance and eventually shortening blade lifespan (Yang et al., 2021).

Regarding particle deposition on turbine blade surfaces, Liu et al. (2021) discovered that the particle deposition on vanes primarily forms near the leading and trailing edge on the pressure surface, and that the deposition area expands slowly to the whole pressure surface with increasing particle size. Hao et al. (2021) observed that particulate deposits in aero-engine turbines alter blade profiles, increase surface roughness, and block internal cooling channels and film cooling holes, thereby degrading aerodynamic and cooling performance. In terms of blade surface roughness, Wang et al. (2019) coated the blade with chromium carbide alloy at high temperature and observed reduced surface roughness and particle deposition. Regarding the effect of deposition on the cooling efficiency of the air film, Sun et al. (2024) pointed out that particle deposition predominantly affects the leading edge and pressure surface of the blade, compromising air film cooling efficiency. However, large-size particles tend to rebound and deposit on the suction surface. In addition to these factors, the blowing ratio also impacts the deposition of the blade surface. Specifically, Zeng et al. (2023) highlighted that particle deposition initially decreases and subsequently increases as the blowing ratio increases from 0.3 to 1.5, with a minimum deposition amount occurring at a blowing ratio of approximately 0.5. Ai et al. (2012a) indicated that the particle deposition rate is not only influenced by the blowing ratio but is also directly correlated with the spanning coverage area of the film cooling. Subsequently,

NOMENCLATURE

A_m	area of a cell	n_i	number of particles impacting wall
$C_{\text{p-1}} = \frac{p_{t,in} - p_{s,l}}{\frac{1}{2}\rho U^2}$	total pressure loss coefficient	n_s	number of particles adhering to the wall
m_d	mass of particle deposition	n_t	total number of injected particles
$m_{d,ave} = \frac{1}{n}\sum_{j=1}^{n} m_{d_j}$	average quality of deposition	$P_d = \frac{n_d}{n_t}$	deposition rate for quantity
m_i	mass of particles impact	$P_{\text{i}} = \frac{n_i}{n_t}$	impact rate for quantity
m_s	mass of particles adhesion	$P_s = \frac{n_s}{n_t}$	adhesion rate for quantity
$m_{s,ave} = \frac{1}{n}\sum_{j=1}^{n} m_{s_j}$	average quality of adhesion	$P_{\text{md}} = \frac{m_d}{m_t}$	deposition rate for quality
m_t	mass of injected particles	$P_{\text{mi}} = \frac{m_i}{m_t}$	impact rate for quality
m_{ad}	mass of particle deposition for a cell	$P_{\text{ms}} = \frac{m_s}{m_t}$	adhesion rate for quality
m_{ai}	mass of particles impact for a cell	$\rho_d = \frac{m_{ad}}{A_m}$	deposition density
m_{as}	mass of particles adhesion for a cell	$\rho_i = \frac{m_{ai}}{A_m}$	impact density
n_d	number of particles deposited on the wall	$\rho_{\text{s}} = \frac{m_{as}}{A_m}$	adhesion density

Ai et al. (2012b) claimed that the deposition rate of turbine blades equipped with thermal barrier coatings is significantly higher than that of conventional turbine blades without such coatings. Wylie et al. (2017) observed that the surface temperature of the turbine blades affects the deposition. Smith et al. (2010) developed an accelerated testing device for the particle deposition in turbine nozzle guide blades. Their findings indicated that with increasing turbine inlet temperature, a greater number of particles are deposited on the blade surface.

Particle deposition on the inter cooling channels of turbine blades was also explored. Specifically, Dritselis (2017) demonstrated that particle deposition on rough walls increases significantly in turbulent channels. This finding is particularly relevant to internal cooling channels of turbine blades featuring spoiler columns and spoiler ribs. Cowan et al. (2010) conducted an investigation into the migration and deposition characteristics of sand-ash particles within the spoiler column array. The findings revealed decreased deposition mass with increasing Stokes number of the particles. Singh et al. (2014) predicted the characteristics of particle deposition in ribbed channels and discovered that the rib wall facing the airflow impingement hole is particularly vulnerable to impact, leading to a heightened likelihood of deposition and erosion. Li et al. (2019) observed significant particle deposition on the rib wall and curved wall within the cooling channel, particularly on the windward side rib wall and the upstream section of the curve. In addition, for cooling channels of other characteristics, Liu et al. (2020) examined the mechanisms by which corrugated cooling channels capture particles. Their findings revealed that the deposition distribution of particles on the channel wall exhibits periodic variation along the flow direction. Cardwell et al. (2010) discovered that the impingement holes located in the cooling channels of double-walled blades effectively filter the particle size on the impact target surface. Borello et al. (2014) found that particle properties affect particle trajectories and deposition distributions. Dowd et al. (2017) indicated that particles sized between 3 and 20 μm are predominantly deposited in stationary channels, whereas those exceeding 10 μm are more likely to accumulate in rotating channels. Bowen et al. (2019) found that the size of the deposition pile in the impingement cooling structure increases with increasing particle temperature while decreasing with increasing particle velocity.

Obviously, the majority of prior research has concentrated on the particle deposition on the surfaces and inter cooling channels of turbine blades. Excessive particle accumulation within blade cooling channels can substantially impair the cooling performance of turbine blades. To address this issue, it is imperative to identify an appropriate section of the turbine disk cavity prior to the internal cooling channels, thereby allowing for the implementation of specific measures aimed at minimizing particle ingress. Furthermore, this location should be designed for easy removal to facilitate the cleaning of accumulated particles. In terms of cost, replacing a cavity structure is considerably less expensive than replacing the blade. Therefore, it is essential to investigate the behavior of particles within the novel cavity upstream of the pre-

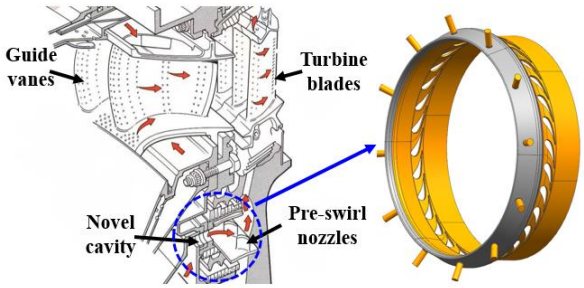

Fig. 1 Novel cavity that upstream of the pre-swirl nozzles

swirl nozzles. This paper proposed for the first time the regulation of particle deposition in the novel cavity upstream of the pre-swirl nozzles. This investigation holds significant importance for minimizing particles ingress into turbine blades, thereby enhancing both turbine blade lifespan and engine viability in dusty environments.

2. METHOD

2.1 Computational Model and Boundary Conditions

The location of the novel cavity upstream of the pre-swirl nozzles within the aircraft engine is illustrated in Fig. 1, with the red arrows denoting the inflow of high-pressure coolant from the engine's air-system. Subsequently, the coolant flowed through the pre-swirl nozzles into the turbine disk cavity and ultimately entered the turbine blades, where it exited through the film holes. Particles were transported by the coolant from the inlet, directed to the target surface through the impingement hole, and then expelled through the pre-swirl nozzles.

The fluid region of the novel cavity upstream of the pre-swirl nozzles presented axial symmetry. The shaft center in the model corresponded to the aircraft engine shaft. From left to right, the model was in the positive direction of the X axis. To streamline the model and optimize computational efficiency, this study employed one-sixth of the entire cavity as the computational domain, taking into account that the airflow at the inlet of the two impingement holes might impact with each other inside the cavity. The plane angle between the two periodic surfaces was set at 60°, as depicted in Fig 2(a). Upon adding the cavity with the baffles, the model is shown in Fig 2(b) to Fig 2(d). The target surface, located on the side of the cavity opposite the impingement hole, features Baffle 1 and Baffle 2. The impact surface, on the same side as the impingement hole, features Baffle 3. In the figure, R_1 is the radius of Baffle 1; R_2 is the radius of Baffle 2; R_3 is the radius of Baffle 3; R_4 is the radius of the impingement hole; L_1 is the distance from Baffle 1 to the upstream stagnation point; L_2 is the distance from Baffle 2 to the upstream stagnation point; L_3 is the distance from the Baffle 3 to the upstream stagnation point; L_4 is the length of the impingement hole channel; L_5 is the length of downstream of pre-swirl nozzles. The radius of R is the distance between the upper surface of the baffle and the engine shaft. Baffle 1 is positioned 0.5 times the diameter

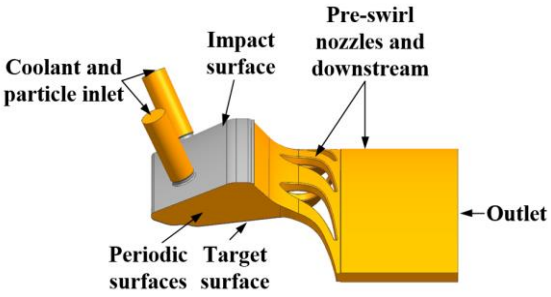

(a) Original structure

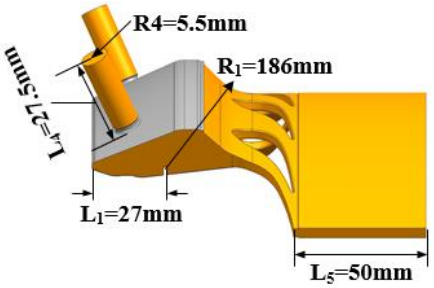

(b) One baffle

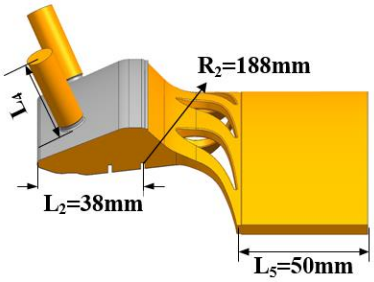

(c) Two baffles

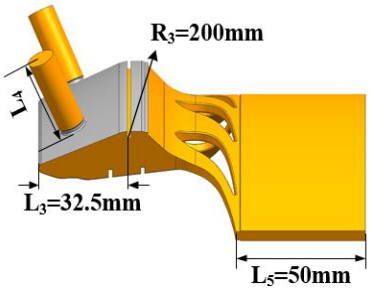

(d) Three baffles

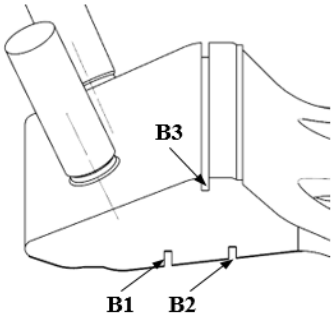

(e) Partial enlarged view of the cavity

Fig. 2 Model diagram of cavity

Table 1 Boundary conditions

Parameter	Value
Total mass flow rate m_p	0.2475 kg/s
Coolant velocity U	100.7m/s
Inlet total temperature $T_{t,in}$	763.5K
Walls temperature T_w	700K
Outlet static pressure $P_{s,out}$	2MP
Turbulence intensity T_u	2%

Table 2 Material properties of particles

Parameter	Value
Particle density ρ_p	1980kg/m^3
Specific heat C_p	984 J/(kg·K)
Thermal conductivity k	0.5 W/(m·K)
Minimum diameter d_{min}	0.2μm
Maximum diameter d_{max}	5μm
Average diameter d_{ave}	2μm

of the impingement hole downstream from the center of the target surface area directly opposite the impingement hole. Baffle 2 is located at the most downstream X-axis coordinate position on the target surface, corresponding to the impact surface. Baffle 3 is situated at the X-axis coordinate position between Baffle 1 and Baffle 2. The thickness of the baffle is 1.5mm. The length of the cavity after the pre-swirl nozzle is L_5=50mm. B1, B2, and B3 represent Baffle 1, Baffle 2, and Baffle 3, respectively.

Numerical simulations were hereby performed utilizing the commercial computational fluid dynamics software FLUENT 2021R1, and the discrete phase model (DPM) was utilized. The computational domain comprised a tetrahedral mesh generated using the Fluent meshing software. The periodic surfaces were designated as rotational periodic boundaries. The Reynolds-averaged Navier-Stokes equations, along with the SST k-ω turbulence model, were employed to resolve the velocity and thermal fields of the continuous phase using the Euler method. The SST k-ω model performs better in the near-wall region and low Reynolds number flow, and more accurately simulates the turbulent characteristics in the boundary layer. Moreover, the small particle size and low deposition height investigated in this study are crucial for understanding particle movement and deposition behavior near the wall. The boundary conditions are provided in Table 1.

The fluid type was hereby defined as an ideal fluid. Each of the two coolant inlets had a mass flow rate of 0.12375 kg/s. The coolant velocity, calculated from the mass flow rate and inlet cross-sectional area, was 100.7 m/s.

The DPM tracked particles uniformly released from inlet after the flow field reached convergence. The particles were modeled as hard spheres and simplified to point masses at the sphere centers. One-way coupling was adopted, and the diameter exhibited a logarithm Rosin-Rammler distribution. The particles' velocity and temperature were identical to those of the coolant. The material properties of the particles are presented in Table 2.

2.2 Particle Force Analysis

The forces acting on particles within the fluid primarily consist of the drag force (F_d) induced by the relative motion between the particles and the fluid, particularly pronounced in the boundary layer; as well as Saffman lift (F_s) and thermophoretic force (F_t) arising from velocity and temperature gradients.

Equations governing the motion of these particles could be expressed as:

$$m_p \frac{du_p}{dt} = F_d + F_s + F_t \tag{1}$$

$$F_d = \frac{1}{2}\rho(u-u_p)^2 A_{cp} C_d \tag{2}$$

$$F_s = 1.615\mu u_p^2 \sqrt{\frac{k_r}{v}}(u-u_p) \tag{3}$$

$$F_t = -D_{T,P}\frac{1}{T}\nabla T \tag{4}$$

where m_p is the mass of the particle, A_{cp} is the particle's front area, k_r is the local velocity gradient, and u and u_p represent the velocities of the fluid and particles, respectively. Meanwhile, μ represents the dynamic viscosity of the fluid, v denotes the kinematic viscosity of the fluid, and ρ indicates the density of the fluid. C_d is defined as the drag coefficient of the particle, while $D_{T,p}$ refers to the thermophoretic coefficient.

2.3 Particle Deposition Model

Brach and Dunn's critical velocity deposition model, based on the dynamic behavior of particles impacting with the wall, effectively describes the rebound or deposition phenomenon of particles after impact. Herein, this model was considered suitable for the particle-wall interaction scenario in this study to judge the adhesion of particles by the critical velocity. Consequently, the critical velocity deposition model proposed by Brach and Dunn (1992) was utilized in this paper, and two distinct processes were carried out. The first process involved the adhesion or rebound of particles upon contact with the wall. Key parameters were defined in accordance with the following equations:

$$v_{cr} = \left(\frac{2E}{d_p}\right)^{10/7} \tag{5}$$

$$E = 0.51\left[\frac{5\pi(k_1+k_2)}{4\rho_p^{3/2}}\right]^{10/7} \tag{6}$$

$$k_1 = \frac{(1-v_s^2)}{\pi E_s} \tag{7}$$

$$k_2 = \frac{(1-v_p^2)}{\pi E_p} \tag{8}$$

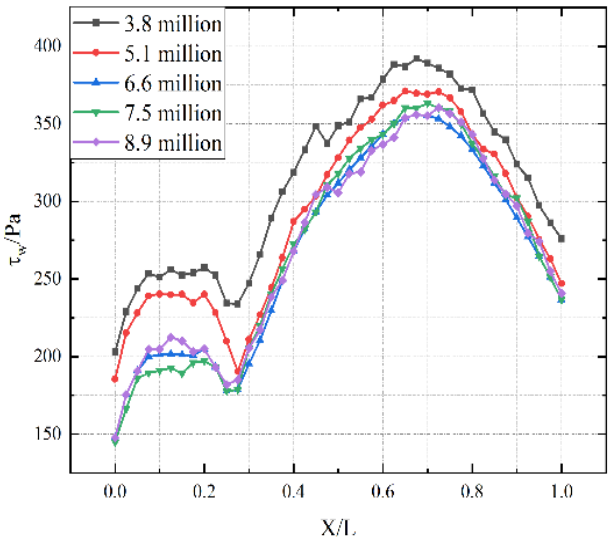

Fig. 3 Shear stress on the target surface under different mesh numbers

where v_{cr} denotes the critical capture velocity of the particles, and E_p and E_s represent the Young's moduli of the particle and wall, respectively. The Poisson's ratios for both the particle and wall are denoted as v_p and v_s, with values of 0.27 for each (Soltani & Ahmadi, 1994). When the normal impact velocity of the particle was below its critical capture velocity (v_{cr}), the particle adhered to the wall. Conversely, if the velocity exceeded the critical capture velocity (v_{cr}), the particle rebounded and continued to move until it exited the computational region or adhered to other walls. According to the experimental studies of Walsh and Ai et al. (Walsh et al., 1990; Bryant & Hurst, 2003; Ai & Kuhlman, 2011), the empirical equation applicable to the Young's modulus of particles were defined in accordance with the following equation:

$$E_p = 3\times10^{18}\exp(-0.03165T_{avg}) \tag{9}$$

It was approximated that the Young's modulus on the deposition surface was the same as the Young's modulus on the particle surface, E_p=E_s. T_{avg} was hereby taken as the average value of the coolant temperature and the wall temperature.

The second process involved the deposition or detachment of particles from the wall after they adhered to the wall. When particles adhered to the wall, some of these particles might be detached from the wall, influenced by the force of the mainstream airflow. This phenomenon was the detachment process. The ability of particles to be detached from the wall was influenced by the combined effects of the force applied by the fluid on the particles and the adhesion the wall for the particles. The adhesion of particles to the wall primarily arose from van der Waals forces. According to EI-Batsh and Haselbacher (2002) from the van der Waals forces acting on particles, the critical shear velocity necessary for particle detachment from the wall was hereby defined in accordance with the following equations:

Table2 Boundary conditions

Number of meshes	5.1million	6.6million	7.5million
Deposition rate	66.41%	66.43%	66.42%

$$u_{\tau c} = \sqrt{\frac{CW_A}{\rho d_p}\left(\frac{W_A}{d_p K}\right)^{1/3}} \tag{10}$$

$$C = 1 + K_n\left(1.2 + 0.41e^{\frac{-0.88}{K_n}}\right) \tag{11}$$

$$K = \frac{4}{3}\left(\frac{1-v_s^2}{E_s} + \frac{1-v_p^2}{E_p}\right)^{-1} \tag{12}$$

$$u_f = \sqrt{\tau_w / \rho} \tag{13}$$

where W_A is the adhesion work, C is the Canning correction coefficient, K_n is the Crusen number, K is the composite Young's modulus, τ_w is the wall shear stress, and ρ is the density of the fluid. Particle detachment or deposition was hereby determined by comparing the wall friction velocity (u_f) with the critical shear velocity ($u_{\tau c}$). If the wall friction velocity exceeded the critical shear velocity, particles were detached. Conversely, particles were deposited.

2.4 Mesh Independence Validation

Herein, the mesh independent verification was conducted on the original structure. The variation of the average shear stress on the target surface with the flow direction is illustrated in Fig. 3. Once the mesh count reached 6.6 million, the average shear stress curve for the target surface exhibited only slight fluctuations. Consequently, it was determined that an optimal mesh number of approximately 6.6 million should be employed. The impact, adhesion, and deposition of particles were determined using the UDF function. Consequently, the deposition rate of particles was independent of the number of meshes, as shown in Table 2. The GCI value was small (0.7%), indicating that the particle deposition rate stabilized with mesh refinement.

3 Results and Discussion

During particle deposition, a coupled approach involving particle input, flow field changes, and migration trajectory changes was employed. After calculating 30 flow fields for every time particle input, the wall state stabilized. The mass of particles one time was 1.97×10^{-7} mg, respectively, and a total of particles 100 times were put into the simulation calculation. Considering not significant deposition characteristics of the impact surface and the pre-swirl nozzles and the downstream area, only the deposition characteristics of the target surface were studied in the contour analysis.

3.1 Deposition Characteristics of the Novel Cavity

The impact, adhesion, and deposition were described by the impact rate, adhesion rate, and deposition rate, respectively. Figures 4 and 5 present the impact rate,

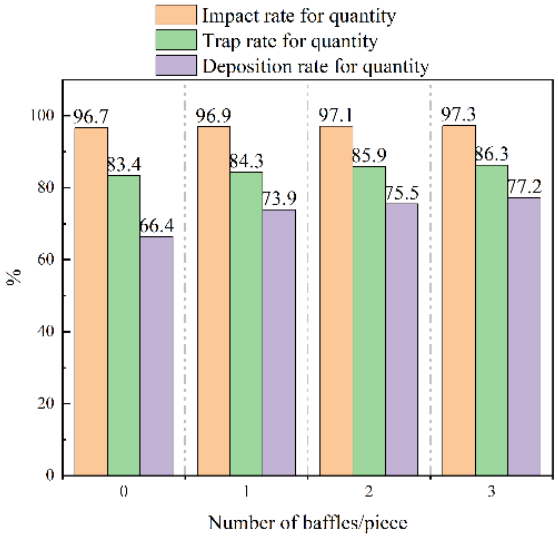

Fig. 4 Quantity-based histogram

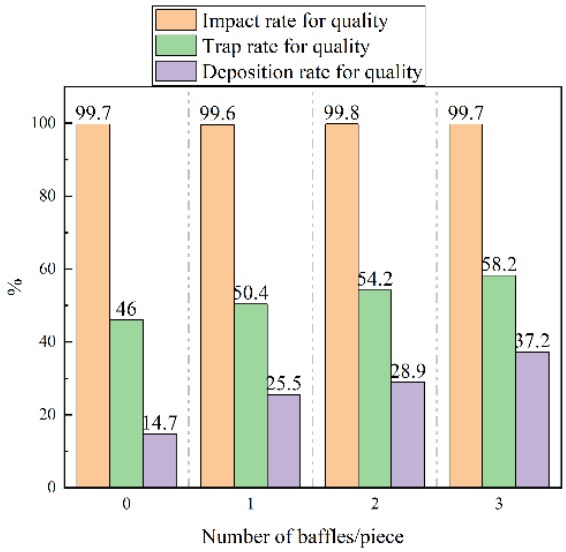

Fig. 5 Quality-based histogram

adhesion rate, and deposition rate changing with the number of baffles based on quantity and quality, respectively. It was observed that with increasing number of baffles, the impact rate for quantity exhibited a slight upward trend. In contrast, the impact rate for quality remained relatively constant. Notably, over 95% of the input particles collided with the wall, yielding a near 100% impact rate by mass. The results indicated that as the number of baffles increased, more small-sized particles that previously did not collide with the wall surface began to do so. Given that these small-sized particles possessed lower mass, the overall impact rate for quality remained relatively unchanged. After the particles collided with the baffle, they lost a portion of their kinetic energy, leading to a reduced velocity. Consequently, the normal impact velocity of the particles was more likely to fall below the critical capture velocity, resulting in increased adhered particles. Therefore, as the number of baffles increased,

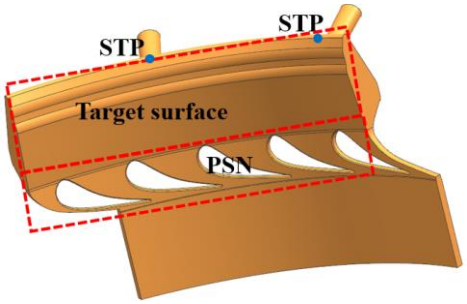

Fig. 6 Position of the target surface

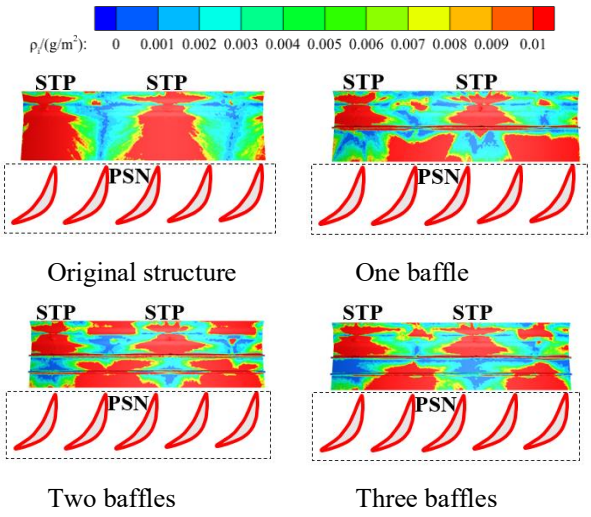

Fig. 7 Impact density of target surface

the adhesion rate for both types gradually improved. The frequency of deposition increased with the number of particles adhering to the surface. This occurred because the deposition mechanism remained unchanged, resulting in an increase in both deposition rates. Compared to the two adhesion rates, the two deposition rates were significantly reduced, indicating that after particles adhered to the wall, some of them detached and ultimately escaped through the outlet. The adhesion rate for quantity was significantly higher than that for quality, and the deposition rate for quantity far exceeded that of quality. This indicated smaller particle-size of adhesion and deposition, and the large particles were more likely to escape with the coolant.

Figure 6 shows the position of the target surface in the model, where STP represents the upstream stagnation point, and PSN indicates the pre-swirl nozzles. Figure 7 presents the impact density contours of the target surface of the four cavities in the X-Y plane. Obviously, the particles initially impacted the target surface area directly opposite the impingement hole, then progressively dispersed and diminished in intensity to the surrounding regions, centered on this initial impact area. Ultimately, the impact density decreased gradually along the flow direction. Combined with the airflow trace distributions and the velocity contours of airflow analysis in Fig. 8, it was observed that the coolant carried particles rushing to the target surface upon injection in the original structure.

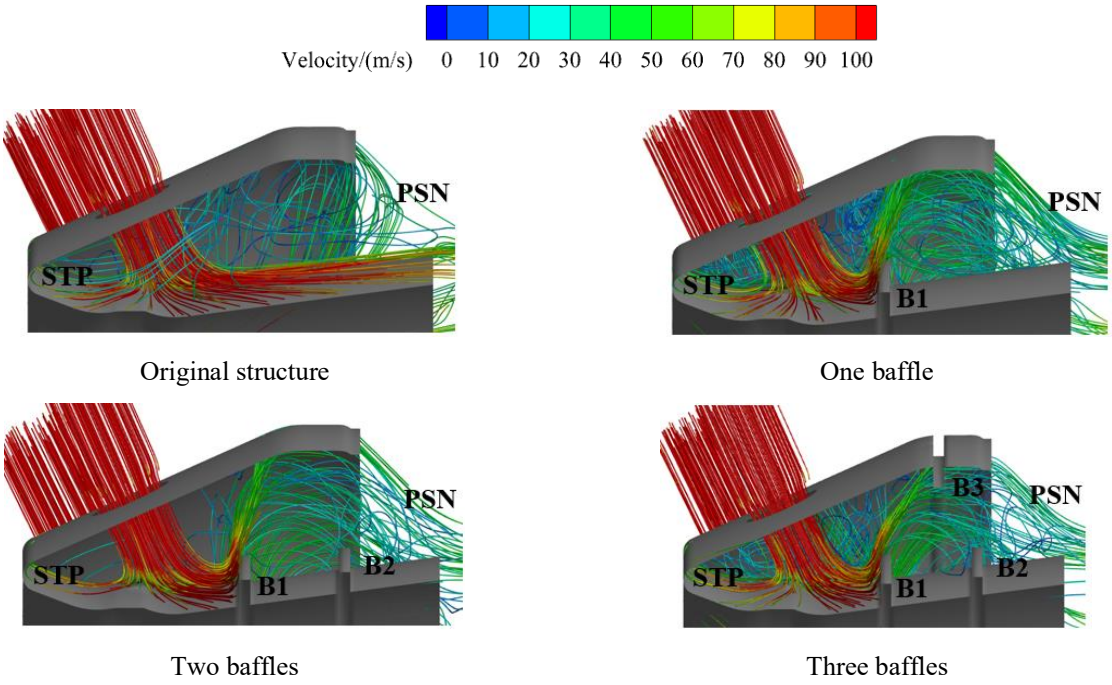

Fig. 8 Airflow traces

This resulted in a high impact density at the target area directly opposing the impingement hole. Subsequently, a portion of the coolant carrying particles continued to flow downstream along the target surface, while another portion rebounded back to the impact surface upon impacting with it. This rebound increased the impact density at the impact surface, which then flowed downstream along the impact surface. It subsequently intersected with the airflow moving along the target surface downstream, ultimately transporting the particles to the pre-swirl nozzles and downstream. The airflow velocity significantly decreased when passing through the upstream stagnation region intersecting the target and impact surfaces, leading to the formation of vortices. Moreover, the impact, adhesion, and deposition of the particles would appear locally dense or sparse, so that the impact density, adhesion density, and deposition density of the particles exhibited uneven distribution in space. For cavities featuring one or two baffles, the presence of these obstructions altered the direction of airflow on the target surface, increasing the amount of coolant carrying particles toward the impact surface. Then, airflow continued to flow downstream along the impact surface. For the cavity equipped with three baffles, Baffle 3 was positioned on the impact surface. As the coolant approached this surface, it collided with Baffle 3, thereby altering its flow direction. The obstructive effect of the baffle led to a generally higher particle impact density near the Baffle 3 area. Due to the intersection of the airflow in the most downstream of the target surface, the impact density of the most downstream particles on the target surface was high and widely distributed.

Figure 9 shows the adhesion density contours of the target surface of the four cavities in the X-Y plane. As

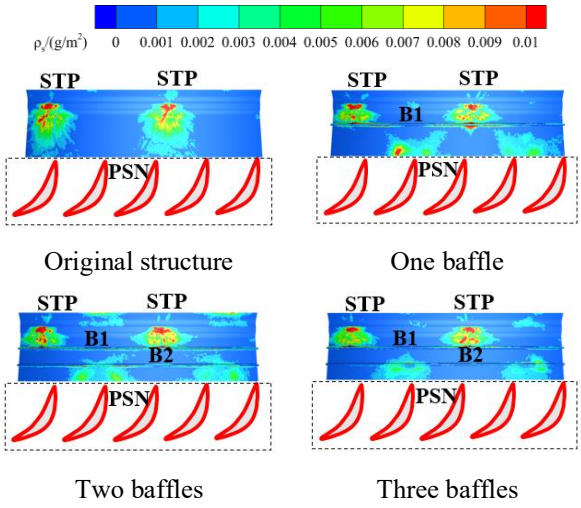

Fig. 9 Adhesion density of target surface

shown in the figure, the adhesion distribution of the target surface resembled the impact distribution, and the area of particles adhesion was basically included in the particles impact area. Furthermore, the adhesion density was significantly smaller than the impact density, indicating that when a majority of particles collided with the wall, their normal impact velocity exceeded the critical capture velocity, leading to a greater number of particles rebounding instead of adhering. For the target surface, their velocity decreased when particles collided with the baffle. Consequently, a greater number of particles adhered to the baffle, thereby resulting in an increased adhesion density on the cavity target surface equipped with one baffle compared to the cavity target surface of original structure. Contrasting with the cavity with one

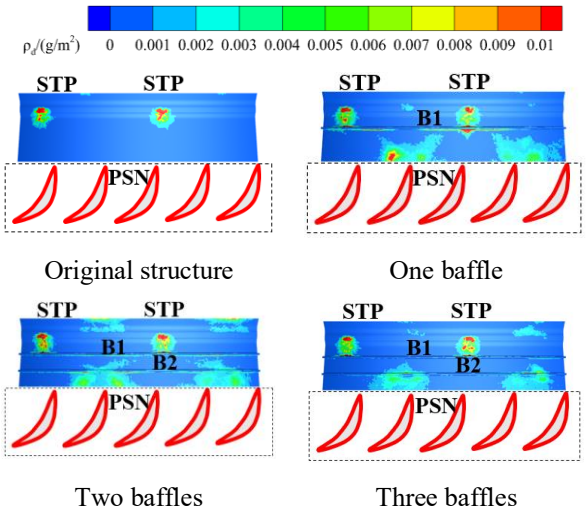

Fig. 10 Deposition density of target surface

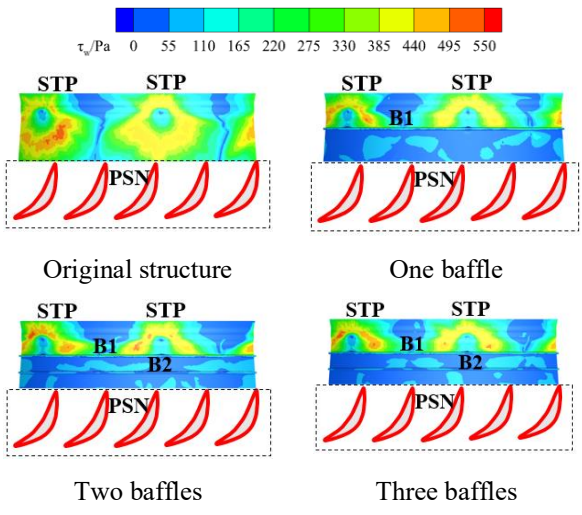

Fig. 11 Shear stress of target surface

baffle, the cavity with two baffles featured an additional baffle positioned downstream of the first. As the airflow transported particles past Baffle 1, some particles impacted Baffle 2 and might adhere between the two baffles. When the particles impacted Baffle 3, some particles adhered, resulting in a higher adhesion density at Baffle 3 compared to other impact surfaces. The airflow traces revealed smaller velocity of the particles carried by the airflow, and it was more likely to adhere, thereby resulting in a higher adhesion density here.

Figure 10 represents the deposition density contours of the target of the four cavities in the X-Y plane. It can be seen that the deposition distribution of particles on the target surface is similar to the adhesion distribution on the whole. Compared with the cavity of original structure, the particles in the cavity with baffles are deposited more on the target surface and are more widely distributed. When one baffle is installed, particles that pass through the baffle continue to move with the airflow or are deposited in other locations. When two baffles are set, a portion of particles will be deposited between the two baffles. The deposition distribution of the cavity with three baffles and the cavity with two baffles is similar on the target surface. Some of the particles will be deposited at the Baffle 3 area. Combined with Fig. 11, the shear stress contours analysis of the target surface of different cavities. For target surface of original structure, the overall shear stress of the wall is larger, the fluid drag moment generated by the wall shear stress exceeds the adhesion moment between the particles and the wall. Particles that have been adhered are less likely to be deposited. The possibility of particles detached is greater. So the deposition density of the target surface is significantly smaller than the adhesion density of the target surface. For the target surface of setting baffles, the shear stress is greater in the upstream region of Baffle 1 and decreases sharply downstream of Baffle 1. This observation indicates that in the area upstream of Baffle 1, there is a significant likelihood that particles adhered to the area will be detached. Conversely, in the downstream area of Baffle 1, particles do not be detached easily after adhered. In the corresponding deposition density contours, the deposition density upstream of Baffle 1 is significantly lower than the adhesion density. In contrast, the deposition density and adhesion density downstream of Baffle 1 are not much different, a finding that can verify with the target shear stress contours.

3.2 Deposition Mass Distribution of the Novel Cavity

Figure 12 shows the variation of the average adhesion quality and the average deposition quality of the target surface along the flow direction. X represents the projection distance in the X-axis direction from any point on the surface to the upstream stagnation point, while L represents the projection length of the target surface or impact surface in the X-axis direction. The average adhesion and deposition quality reached their first peak on the target surface directly opposite the impingement hole (X/L = 0.25–0.3), and the average adhesion qualities of the four cavities were around 4mg/m^2. The average adhesion quality exceeded the average deposition quality, indicating that some particles detached after initial adhesion. The second small peak in the average adhesion quality was observed between the impingement hole directly opposite the target surface area and Baffle 1 (X/L = 0.4–0.42). This region corresponded to a higher particle adhesion density on the target surface, where shear stress was larger, leading to more pronounced detaching phenomena. Consequently, the average deposition quality in this area did not peak and was significantly lower than that of the average adhesion quality. The third peak of the average adhesion quality and the average deposition quality was observed in the root area upstream of Baffle 1 (X/L = 0.5–0.52). For the cavity target surface with one baffle, this peak value was notably higher; and there was no peak value for the cavity target surface of original structure. The peak sizes on the target surfaces of the three baffled cavities were essentially similar. Furthermore, the average adhesion quality across all four cavities exceeded that of the deposition quality, and a small number of particles were detached. In the downstream region behind Baffle 1 (X/L = 0.54–0.6), the cavity target surface with one baffle exhibited peaks in both average adhesion quality and average deposition quality. In contrast, the

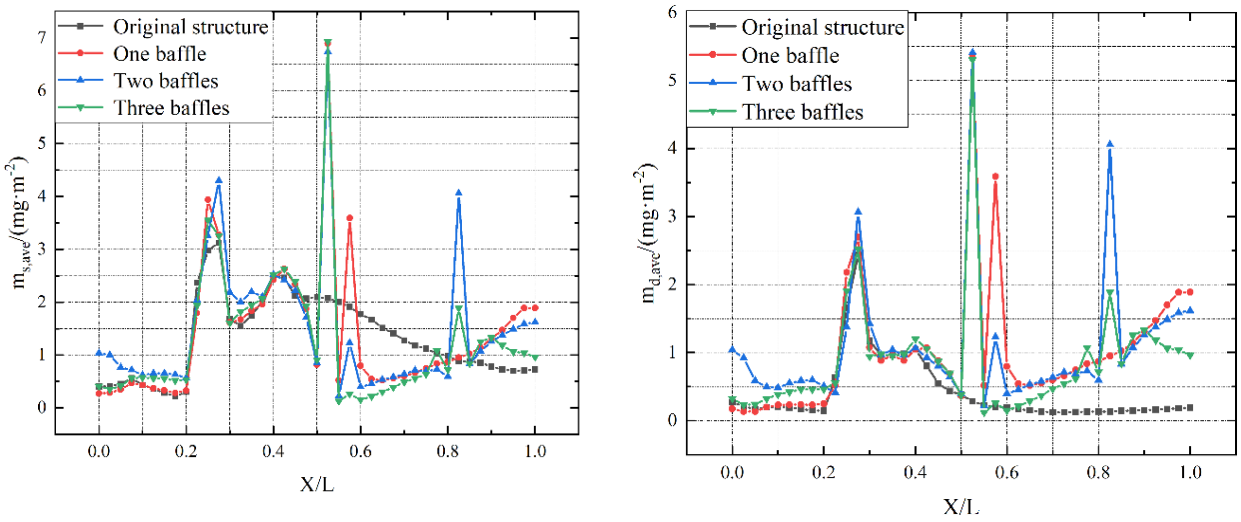

Target surface adhesion　　Target surface deposition

Fig. 12 Variation of the average adhesion quality and average deposition quality of the target surface along the flow direction

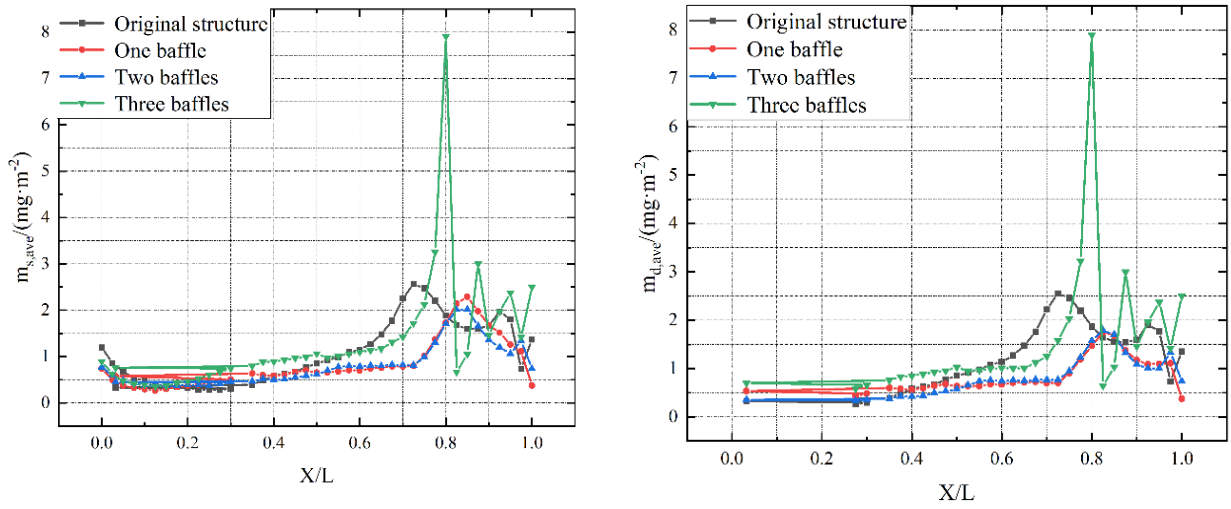

Target surface adhesion　　Target surface deposition

Fig. 13 Variation of the average adhesion quality and average deposition quality of the impact surface along the flow direction

original structure's cavity target surface did not show a peak in average adhesion quality. However, it remained higher than that of target surfaces with two or three baffles. Notably, the wall shear stress dropped sharply downstream of Baffle 1, and it was difficult to be detached for particles. As a result, the average deposition quality of the three cavities with baffles was basically equal to the average adhesion quality. The cavity target surface of the original structure, subjected to high wall shear stress, experienced significant particle detachment, resulting in the lowest average deposition quality, which was considerably lower than the average adhesion quality. In the root area upstream of Baffle 2 (X/L = 0.8–0.85), both the average adhesion quality and average deposition quality of the target surfaces of the cavities with two and three baffles exhibited a peak. Furthermore, the average deposition quality of the three target surfaces of the cavities with baffles was basically equal to the average adhesion quality. In contrast, the average deposition quality of the target surface of the cavity of original structure was significantly lower than the average adhesion quality. Due to the convergence of the downstream airflow (X/L=0.9–1) over the target surface, both the average adhesion quality and average deposition quality were significantly enhanced.

Figure 13 illustrates the variation of the average adhesion quality and average deposition quality along the flow direction on the impact surface. The average adhesion quality and average deposition quality first peaked on the impact surface of the original cavity structure. The airflow initially rebounded from the target

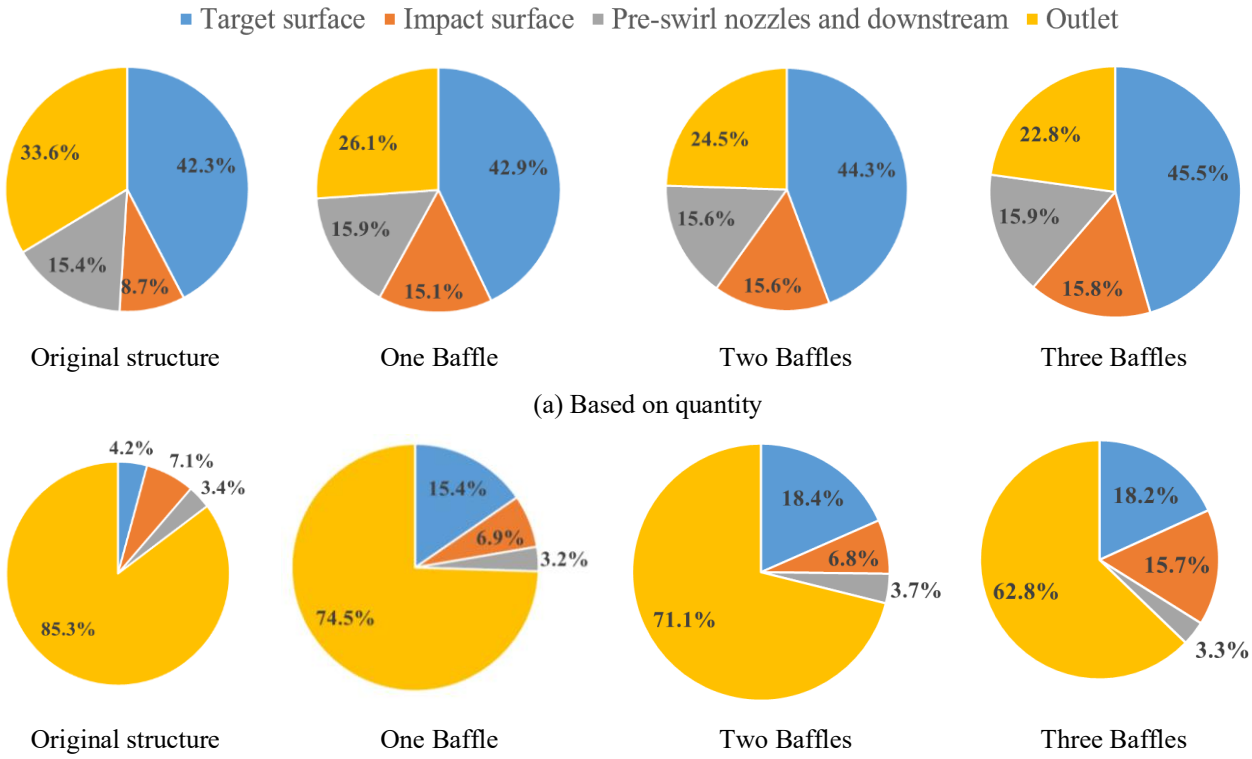

Fig. 14 Proportion of deposition

surface to the impact surface (X/L = 0.7–0.75). For the baffled cavity, the airflow velocity carrying particles and bouncing back to the impact surface was higher due to the influence of Baffle 1. The normal impact velocity of a larger number of particles exceeded the critical capture velocity, making it difficult for these particles to adhere. Consequently, the peak location for the original cavity structure was positioned further upstream compared to that of the baffled cavity. The average deposition quality on the impact surface of the original cavity structure was basically equal to the average adhesion quality, with minimal particle detachment observed. The second peak of the average adhesion quality and average deposition quality was observed on the impact surface of the cavity with three baffles. In the root area upstream of Baffle 3 (X/L=0.79–0.81), a significant accumulation of particles occurred due to the obstruction caused by Baffle 3. Consequently, both the average adhesion quality and average deposition quality in this region were considerably higher than those recorded in the other three cavities. The remaining small peaks were observed in the most downstream region of the impact surfaces. Analysis of the impact and adhesion density contours indicated that repeated particle impacts and adhesions in this area led to the deposition of multiple small hills.

3.3 Proportion of Deposition at Typical Locations

Figure 14 illustrates the percentage of particle deposition by quantity and quality at each section, with the outlet indicating that undeposited particles have exited through it. From a quantitative perspective, the proportion of target surface deposition in the four cavities was observed to be the highest. Furthermore, as the number of baffles increased, the proportion of target surface deposition exhibited an overall upward trend, while that of impact surface deposition was significantly higher compared to the original structure. Given that the pre-swirl nozzles and downstream structure remained unchanged, the flow characteristics of the airflow carrying particles through this region were also consistent. Consequently, the deposition proportion in this area remained essentially stable. As the number of baffles increased, however, the overall deposition rate within the cavity rose correspondingly, leading to a progressively smaller proportion of outlet escape. From a qualitative perspective, the proportion of deposition within cavities with baffles significantly increased compared to the original structure. Conversely, from a quantitative standpoint, minimal change was observed. This indicated that the baffle effectively obstructed a greater number of larger particles. The proportion of target surface deposition did not change significantly for the three baffled cavities. The qualitative deposition proportion on the impact surface of the original cavity structure exceeded that observed in cavities with one or two baffles. Conversely, the quantitative deposition proportion in the cavity of original structure was lower than that found in cavities with one or two baffles. These results indicated that after installing a single baffle on the target surface, the particles rebounding to the impact surface exhibited smaller diameters and higher quantities. In contrast, before baffle installation, rebounding particles were larger in size and fewer in number. Given that the Baffle 3 was positioned on the impact surface, both the quantity and

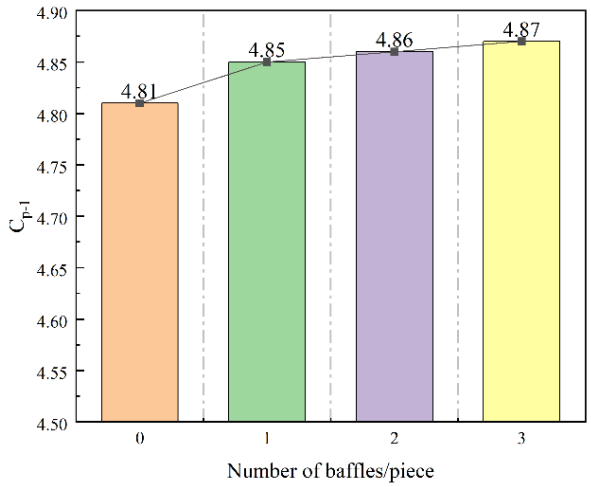

Fig. 15 Total pressure loss coefficients of different cavity structures

quality of the cavity deposited on impact surface were naturally greater, resulting in an increased deposition proportion. From both quantitative and qualitative perspectives, the proportion of pre-swirl nozzles and downstream deposition remained relatively constant, while that of total deposition within the cavity increased with more baffles. Consequently, this led to a gradually decrease in the proportion of particles escaping through the outlet with an increasing number of baffles.

Figure 15 represents a histogram of the total pressure loss coefficient of the four cavities. In the process of increasing the number of baffles from zero to three, the total pressure loss coefficients were recorded as 4.81, 4.85, 4.86, and 4.87, respectively. Based on the total pressure loss coefficient observed cavity of original structure, the total pressure loss coefficients for cavities with 1, 2, and 3 baffles exhibited increases of 0.83%, 1.04%, and 1.25%, respectively, compared to the cavity of original structure. Evidently, the total pressure loss coefficient of the cavity remained relatively unchanged before and after the baffle installation, thereby demonstrating the rationality of the baffle structure. The baffle only slightly increased the complexity and resistance of the flow, altering the flow path of the fluid.

4 CONCLUSIONS

Using the critical velocity deposition model, this study examined how baffle structures affected the migration and deposition characteristics of the novel cavity upstream of the pre-swirl nozzles.

The main conclusions could be listed as follows:

1) With an increasing number of baffles, the quantity-based impact rate, adhesion rate, and deposition rate within the cavity exhibited a corresponding increase. However, the quality-based impact rate remained largely unchanged, while the quality-based adhesion and deposition rates rose.

2) The target surface area directly opposite the impingement hole and the baffles area exhibited significantly broader distributions of impact, adhesion, and deposition compared to other regions.

3) Before and after the installation of the baffles, the deposition rates for quantity within the cavity were recorded at 66.4%, 73.9%, 75.5%, and 77.2%, respectively. These figures corresponded to a reduction in the number of particles entering the turbine disk cavity by 33.6%, 26.1%, 24.5%, and 22.8% respectively. The deposition rates for quality were 14.7%, 25.5%, 28.9% and 37.7%, respectively, corresponding to a reduction in the mass of particles entering the turbine disk cavity by 85.3%, 74.5%, 71.1%, and 62.3%, respectively. Overall, the baffle structure could effectively reduce particle ingress into both the turbine disk cavity and rotor blades.

ACKNOWLEDGEMENTS

The authors gratefully acknowledge the financial support from the National Natural Science Foundation of China (52376028) and the Natural Science Foundation of Liaoning Province of China(2023-MS-245).

CONFLICT OF INTEREST

The authors have no conflicts to disclose.

AUTHORS CONTRIBUTION

Guangchao Li: Funding acquisition, Writing-review & editing; **Yan Wang**: Writing-original draft; **Wei Zhang:** Writing-review.

REFERENCES

Ai, W. G., Murray, N., Harding, S., & Lewis, S. (2012a). Deposition near film cooling holes on a high pressure turbine vane. *Journal of Turbomachinery*, *134*(4), 041013. https://doi.org/10.1115/1.4003672

Ai, W. G., Murray, N., Harding, S., & Bons, J. P. (2012b). Effect of hole spacing on deposition of fine coal flyash near film cooling holes. *Journal of Turbomachinery*, *134*(4), 041021. https://doi.org/10.1115/1.4003717

Ai, W., & Kuhlman, M. J. (2011). Simulation of coal ash particle deposition experiments. *Energy & Fuels*, *5*(10), 2874-2877. https://doi.org/10.1021/ef101294f

Borello, D., Capobianchi, P., Petris, M. De., & Rispoli, F. (2014). Unsteady RANS analysis of particle deposition in the coolant channel of a gas turbine blade using a non-linear model. *Asme Turbo Expo*, *45714*, V05AT12A035. https://doi.org/10.1115/GT2014-26252

Bowen, C. P., Libertowski, N. D., & Mortazavi, M. (2019). Modeling deposition in turbine cooling passages with temperature-dependent adhesion and mesh morphing. *Journal of Engineering for Gas*

Turbines and Power, *141*(7), 071010. https://doi.org/10.1115/1.4042287

Brach, R., & Dunn, P. F. (1992). A mathematical model of the impact and adhesion of microspheres. *Aerosol Science and Technology, 16*(1), 51-64. https://doi.org/10.1080/02786829208959537

Bryant, G. W., & Hurst, H. J. (2003). An empirical method for the prediction of coal ash slag viscosity. *Energy Fuels*, *17*(3), 731-737. https://doi.org/10.1021/ef020165o

Cardwell, N. D., Thole, K. A., & Burd, S. W. (2010). Investigation of sand blocking within impingement and film-cooling holes. *Journal of Turbomachinery*, *132*(2), 021020. https://doi.org/10.1115/1.3106702

Cowan, J. B., Tafti, D. K., & Kohli, A. (2010). Investigation of sand particle deposition and erosion within a short pin fin array. *Turbo Expo: Power for Land, Sea, and Air*, *43994*, 139-149. https://doi.org/10.1115/GT2010-22362

Dowd, C.， Tafti, D., & Yu, K. (2017). Sand transport and deposition in rotating two-passed ribbed duct with coriolis and centrifugal buoyancy forces at Re=100,000. *Proceedings of the ASME Turbo Expo*, 50817. https://doi.org/10.1115/GT2017-63167

Dritselis, C. D. (2017). Numerical study of particle deposition in a turbulent channel flow with transverse roughness elements on one wall. *International Journal of Multiphase Flow, 91*, 1-18. https://doi.org/10.1016/j.ijmultiphaseflow.2017.01.004

El-Batsh, H., & Haselbacher, H. (2002). Numerical investigation of the effect of ash particle deposition on the Flow Field Through Turbine Cascades. *Power for Land, Sea, and Air*, *3610*, 1035-1043. https://doi.org/10.1115/GT2002-30600

Felix, D., Stephan, S., & Christian, K. (2017). Modeling particle deposition effects in aircraft engine compressors. *Journal of Turbomachinery*, *139*(5), 051003. https://doi.org/10.1115/1.4035072

Hao, Z., Yang, X., & Feng, Z. (2021). Unsteady simulations of migration and deposition of fly-ash particles in the first-stage turbine of an aero-engine. *The Aeronautical Journal*, *125*(1291), 1566-1586. https://doi.org/10.1017/aer.2021.27

Li, L., Liu, C., Shi, X. Y., Zhu, H., & Li, B. (2019). Numerical investigation on sand particle deposition in a u-bend ribbed internal cooling passage of turbine blade. *ASME Turbo Expo*, *58585*, V02DT47A007. https://doi.org/10.1115/GT2019-90850

Liu, J., Ji, B., Tang, Z., & Song, Q. (2020). Particle movement behavior and capture mechanism in a corrugated cooling channel. *Powder Technology*, *376*, 380-389. https://doi.org/10.1016/j.powtec.2020.08.064

Liu, Z., Diao, W. N., Liu, Z. X., & Zhang, F. (2021). A numerical study of the effect of particle size on particle deposition on turbine vanes and blades. *Advances in Mechanical Engineering*, *13*(5), 1-12. https://doi.org/10.1177/16878140211017812

Singh, S., Tafti, D., Reagle, C., & Delimont, J. (2014). Sand transport in a two pass internal cooling duct with rib turbulators. *International Journal of Heat and Fluid Flow*, *46*(2), 158-167. https://doi.org/10.1016/j.ijheatfluidflow.2014.01.006

Smith, C., Barker, B., Clum, C., & Bons, J. (2010). Deposition in a turbine cascade with combusting flow. *Turbo Expo: Power for Land, Sea, and Air*, *43994*, 743-751. https://doi.org/10.1115/GT2010-22855

Soltani, M., & Ahmadi, G. (1994). On particle adhesion and removal mechanism in turbulent flows. *Journal of Adhesion Science and Technology*, *8*(2), 763-785. https://doi.org/10.1163/156856194X00799

Sun, W. J., Zheng, Y. Q., Gao, Q. H., & Zhang, J. Z. (2024). Numerical simulations on film cooling performance of turbine blade before and after particle deposition. *Thermal Science and Engineering Progress*, *49*, 102504. https://doi.org/10.1016/j.tsep.2024.102504

Walsh, P. M., Sayre, A. N., Loehden, D. O., & Monroe. L. S. (1990). Deposition of bituminous coal ash on an isolated heat exchanger tube: Effects of coal properties on deposit growth. *Progress in Energy & Combustion Science*, *16*(4), 327-345. https://doi.org/10.1016/0360-1285(90)90042-2

Wang, J. J., Lin, Y. J., Xu, W., Li, Q., & Abhijit, D. (2019). Effects of blade roughness on particle deposition in flue gas turbines. *Powder Technology*, *353*, 426-432. https://doi.org/10.1016/j.powtec.2019.05.045

Wylie, S., Bucknell, A., Forsyth, P., & Gillespie, D. R. H. (2017). Reduction in flow parameter resulting from volcanic ash deposition in engine representative cooling passages. *Journal of Turbomachinery*, *139*, 031008. https://doi.org/10.1115/1.4034939

Yang, X., Hao, Z., & Feng, Z. P. (2021). An experimental study on turbine vane Leading-Edge film cooling with deposition. *Applied Thermal Engineering*, *198*, 117447. https://doi.org/10.1016/j.applthermaleng.2021.117447

Zeng, J. W., Wang, F. L., Wang, Y. Q., Wang, Y. B., & Shi, J. (2023). Particle deposition characteristics on turbine blade surface based on critical velocity model. *Journal of Physics: Conference Series*, *2610*(1), 1742-6596. https://doi.org/10.1088/1742-6596/2610/1/012041